Mechanical behavior of AZ31B magnesium alloy under conditions of in-plane biaxial fatigue

R. Cruz

ricardo.s.cruz@tecnico.ulisboa.pt

Instituto Superior Técnico, Universidade de Lisboa, Portugal

ABSTRACT

In the present work, the mechanical behavior of AZ31B-H24 magnesium alloy to in-plane biaxial fatigue was investigated. For such, tension-controlled multiaxial fatigue experiments were conducted on cruciform specimens, geometrically optimized to test on a biaxial testing machine developed internally. The fatigue tests were performed with sinewave loads for in-phase and out-of-phase cases, keeping a constant load ratio and a null mean stress. The experimental tests were complemented with data from numerical simulations in ABAQUS commercial software. A few critical planes multiaxial fatigue criteria were evaluated in terms of crack initiation and life prediction based on the experimental results. From the several models studied, only the models that define the critical planes based on normal stresses and extensions provided good estimations for crack initiation angle. For specimen's life prediction, the best results were obtained by minimum circumscribed ellipse (MCE) and Liu I criteria. The crack propagation study obtained, acceptable Paris' law constants, through numerical and experimental data correlation, considering previous studies conducted in similar magnesium alloys.

KEYWORDS: Magnesium alloy, fatigue test, numerical simulation, cruciform specimens

1. Introduction

Several industries, such as automobile, aircraft, sport or even medical, are in constant demand for lower density materials that also present good structural properties. This is where the magnesium alloys enter. Magnesium alloys are one of the lightest alloys available with high specific strength and excellent machinability. In automobile and aircraft sector, the generalization of magnesium presents even more benefits due to the reduction of fossil fuels consumption [1].

Most of magnesium applications make use of cast components with little or no structural function. However, cast Mg alloys present flaws like casting pores and inclusions, where wrought ones are free of casting defects. Therefore, in recent years, wrought Mg alloys have come forward as candidates for structural applications.

Structural components are subjected to all kinds of loads, basic, complex, constant and cyclic ones. Although, the main cause of mechanical structures collapse is due to fatigue phenomena, in consequence of damage accumulation of cyclic loads [2]. With the present scenario, it is of crucial importance understanding Mg alloy behavior to fatigue.

Past studies have been preferably conducted at uniaxial tests, for instance, the works of Yu and Chen [3] [4], despite structural components usually experiencing multiaxial loads. In these conditions, studies have been limited to a few Mg alloys, tension states and loading histories [5] [6].

The present document investigates the behavior of rolled AZ31B Mg alloy under conditions of in-plane biaxial fatigue. Thus, several fatigue tests were conducted and afterward correlated with finite element models' data. The crack growth on the specimen was monitored throughout the various tests and then characterized based on Paris' law. Also, a few critical planes criteria were applied, namely Findley, modified Smith-Watson-Topper (SWT) and Liu criteria, in order to evaluate their feasibility to estimate crack behavior and fatigue life of the alloy. To the previous ones, the study was complemented with the Minimum Circumscribed Circle (MCC) and Minimum Circumscribed Ellipse (MCE), since these proved to be quite efficient in life prediction to in-plane biaxial fatigue, according to Fonseca's study [7]. The Fatemi-Socie criterion was not studied as in Yu's study [5], conducted for a AZ61A magnesium alloy, it presented poor quality results.

2. Material and specimens

The material used in current investigation is a AZ31B-H24 magnesium alloy supplied in the form of a 3.15mm thickness sheet. This material possesses a chemical composition in weight percentage of 2.5-3.5 Al, 0.60-1.4 Zn, 0.2 Mn, 0.01 Si, 0.05 Cu, 0.04 Ca, 0.005 Fe, 0.005 Ni, and Mg as balance.

Table 2.1 – Material's properties

Grain orientation	0º	45º	90º
Yield Tensile Strength (MPa)	200	200	210
Ultimate Tensile Strength (MPa)	222	223	236
Young's Module (GPa)	43,6	41,5	40,6
Shear Modulus (GPa)	15		16,1
Poisson's coefficient	0,4	0,4	0,4

Table 2.2 – Specimen's dimensions

rr (mm)	RM (mm)	Rm (mm)	dd (mm)	t (mm)	tt (mm)	Θ(º)
7,5	63,2	20,4	51	3,2	0,4	21

However, as the material designation suggests, the letter B indicates that this alloy differs slightly in composition.

To complement the material's data with its behavior with loads, it was performed hardness and tensile tests. Vickers hardness tests exhibited a range of results between 69 to 72 HV, both along the roll direction and along the transverse direction. The results obtained in the tensile tests are presented in table 2.1 according to grain direction. The tensile specimens tested presented grain orientation parallel to load direction (DL) and inclined in 45º and 90º to DL. The tests were conducted by EN10 002-1 norm.

Specimens tested to in-plane biaxial fatigue are cruciform shaped containing a small central circle of reduced thickness, figure 2.1.
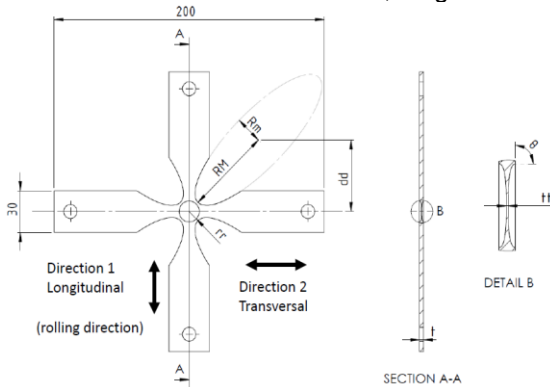

Figure 2.1 – Specimen's geometry

To consider material texture, specimens with grain orientation parallel to load direction and inclined in 15º to DL were tested. The detailed geometry of these specimens has been optimized in several studies [8] [9], from which were obtained several sets of dimensions that proved to be optimum to the imposed conditions and objectives, through Direct multi-search (DMS) method. From these objectives, the main ones served to guarantee that maximum tension appeared at the center of the specimen, that the center tensions were uniformly distributed and that arms' tensions were reduced. These conditions confer to the specimen favorable characteristics to crack initiation, despite the relative low loads.

Of the design variables that define the specimen's geometry, two are kept constant in order to ensure the minimum dimensions supported by the biaxial machine and monitorize the magnesium sheet, namely, the length and width of specimen's arms with values of 200 and 30mm, respectively. Also, to assure good machinability, the specimen's center thickness tt takes into account the minimum stipulated value of 0.5mm [10]. Considering these constrictions, all design variables values are presented in table 2.2.

All specimens were manufactured in two separate stages. First stage provided a general shape by abrasive waterjet machining, in order to avoid contamination with thermally affected spots, residual tensions and burrs. Second stage reached the intended final geometry trough CNC milling machine, which confer great precision. The specimen machining ends in center polishing with sandpapers from P600, P800, P1000 to P2500 and a final diamond abrasive of 3μm.

3. **Equipment**

All experimental fatigue tests were conducted in a Biaxial Testing Machine (BTM), figure 3.1, which was developed by Instituto Superior Técnico in collaboration with Instituto Politécnico of Setúbal. This machine is composed by four linear motors arranged crosswise, assuring symmetry and preventing specimen's center dislocation during test. The motors are controlled independently by force, extension and dislocation, through controllers based on an aluminum structure that share no contact with the rest of the machine. This system combines air bearings and lateral

guides with rollers that establish a horizontal planar movement free of friction [11].
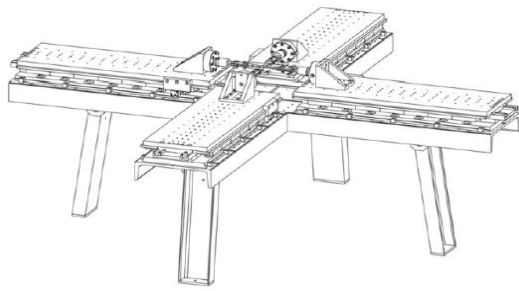

Figure 3.1 – BTM machine

The progression of experimental tests was monitored by a VEHO VMS-001 200x USB microscope, that working in tandem with the software interface of BTM, takes a picture on pre-defined gaps set by the user. Configured with an ampliation of 20x, this assembly was responsible for taking and saving all photos in each 2500 cycles. Thus, it allowed to identify the cycles at which crack initiated and at which specimen collapsed, keeping a close track of crack propagation.

4. Numerical simulations

For this study, simulations of finite element models assume extreme importance as it provides values for tension, extension and stress intensity factor (SIF) at specimens' center. For each tested specimen was created a finite element model (FEM) using software ABAQUS, with the goal of obtaining results as close to reality as possible. These models were created with tested specimens' real dimensions, except for thickness which was reduced to half as commitment to decrease computational processing time. The material AZ31B was defined as orthotropic, in ABAQUS command as "Engineering constants" once characterize Young's modules and Poisson's coefficients in principal direction was enough, table 2.1. The established parameters describe material behavior depending on grain orientation. As referred previously, this study tests specimens with grains oriented along 0º and 15º to the load direction. This way it is necessary create two vector systems, one is the origin axis system, where grain is oriented along Y-axis and another where X and Y-axis are slightly deviated with an 15º angle in relation to the origin system.

In order to compute SIF at crack front for different crack sizes obtained at several instants from the monitoring of crack growth, specimens with crack were modelled. To simulate an ideal crack behavior, both crack tips were defined by small circles $\emptyset = 0.02$ mm, partitioned into quarters. As ABAQUS software only recognizes

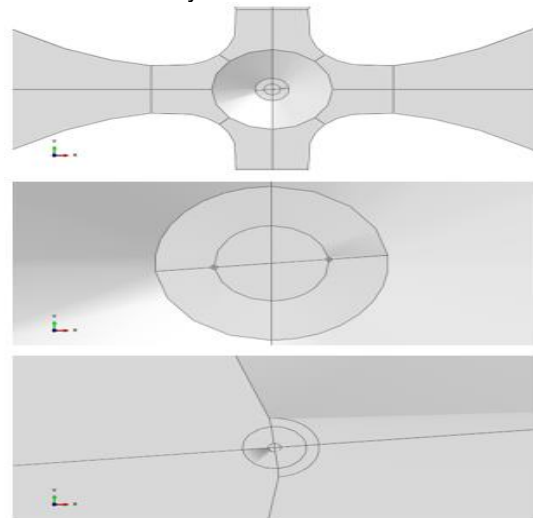a crack front singularity, it was necessary to model two to fully describe the crack.

Figure 4.1 - Singularity' detail

Construction of the mesh was based on the next main concerns, guaranteeing regulars transitions, coherent results and reasonable computational time. Most of specimen's mesh was modelled with brick elements (C3D20R), except for crack tip that was generated with wedge elements (C3D15) which enables a better characterization of this singularity. All these elements are 3D solids of quadratic geometric order. The resulting mesh is composed of 27432 elements with 128204 nodes. Figure 4.2 describes the regularity of mesh transitions as representation of the detail encountered at crack tip.
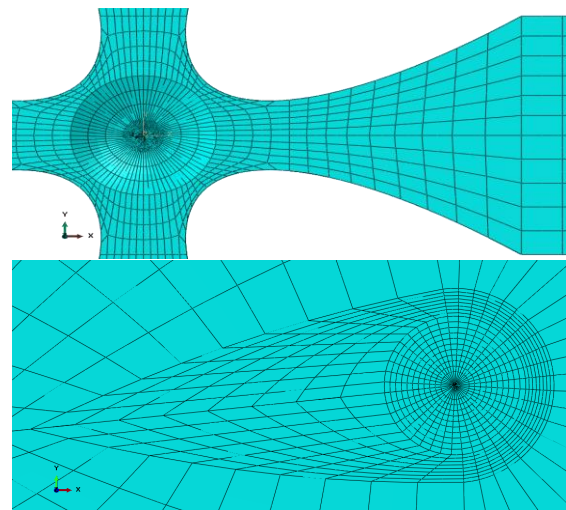

Figure 4.2 – FEM mesh

To ensure that both FEM and the experimental specimens were under the same conditions, boundary conditions were applied. In experimental case, all specimens' arms are subjected to symmetrical cyclic loads. However, in order to simplify the simulation in ABAQUS

3

software, it was defined that force would only be applied to one arm in each direction. Thus, it was necessary to restrict any movement at the tip of the opposing arms. Since no specimen movement along the Z-axis was also desired, the bottom flat face of the model was restricted. Finally, to complete the boundary conditions, it was ensured that there was no displacement in the center of the model.
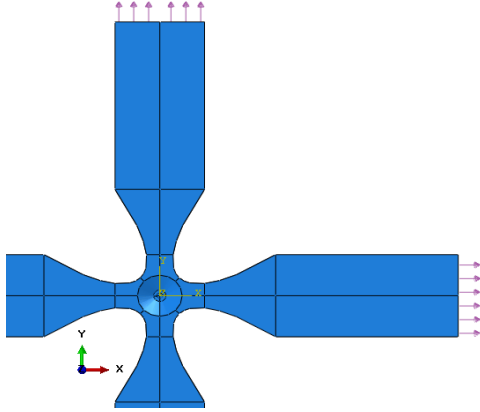

Figure 4.3 – Applied loads

Both loads were applied in a single step with increments of 0.05 so as to represent a complete load cycle, defined by sine functions (1) and (2), with fair precision.

$$F_1 = F_a.\sin(wt) \qquad (1)$$

$$F_2 = F_a.\sin(wt + \delta) \qquad (2)$$

Where F_a corresponds to load amplitude, F_1 and F_2 to applied load along direction 1 and 2 respectively. The parameter w is the frequency, t is the time and δ is the phase between both loads.

Once the stress intensity factor (SIF) is dependent on geometry and crack size, it was necessary to collect the SIF along crack propagation. Thus, several specimens were modeled based on t photographs taken during fatigue test. For each FE analysis, the SIF was collected for three contours at each increment.

Although the applied loads mostly caused mode I damage, mode II was also felt. This way, in order to calculate SIF equivalent, it was applied the model suggested by Richard [12]:

$$K_{eq} = \frac{K_I}{2} + \frac{1}{2}\sqrt{K_I^2 + 4(1.155K_{II})^2} \qquad (3)$$

With K_I and K_{II} being the stress intensity factors for fracture modes I e II, respectively. The range of values of K_{eq} can be obtained by the difference between the maximum and the minimum values of K_{eq} for a loading cycle:

$$\Delta K_{eq} = K_{eq,max} - K_{eq,min} \qquad (4)$$

5. Multiaxial fatigue criteria

In order to predict specimen's life, it is essential to determine the damage parameter of each model, DP. Afterwards, through interpolation of S-N or ε-N points from a potential trend line, it is determined the number of cycles to fracture 2N.

$$DP = \lambda(2N)^b \qquad (5)$$

To obtain the critical plane it is necessary to scan all planes to achieve the maximum combination of DP.

5.1. Findley

Findley's criteria combine the maximum alternating shear stress on the critical plane with the respective normal stress of the following equation:

$$DP = \left\{\frac{\Delta\tau}{2} + k\sigma_n\right\}_{max} \qquad (6)$$

Where $\Delta\tau$ is shear stress range, σ_n is normal stress and k is a model's constant.

5.2. Modified SWT

SWT criterion suggests that fatigue life is controlled by crack propagation in planes perpendicular to the maximum principal stress or strain. This criterion is a critical plane model, which in multiaxial loading is based on the amplitude of principal extension $\Delta\varepsilon_1$ and the maximum tension of the corresponding plane $\sigma_{n,max}$:

$$DP = \sigma_{n,max}\frac{\Delta\varepsilon_1}{2} \qquad (7)$$

To the criterion presented, Jiang and Sehitoglu [13] elaborated modifications in order to consider the general behavior of the crack. The modified SWT criterion can be expressed according to:

$$DP = 2b.\Delta\varepsilon.\langle\sigma_{max}\rangle + \frac{1-b}{2}\Delta\tau.\Delta\gamma \qquad (8)$$

Where σ and τ is the normal and shear stress in a plane of the material, respectively. ε and γ is the extension and the distortion corresponding to the normal and shear stress, respectively. The $\langle \rangle$ symbol is the parentheses of MacCauley that is defined by equation $\langle x \rangle = 0.5 \times (x + |x|)$, which ensures that no negative damage can be produced. b is a material constant ranging from 0 to 1.

5.3. Liu I and Liu II

The Liu's criterion is a critical plane model based on virtual strain energy (EVD), which calculates the elastic and plastic work of specific planes. The maximum value obtained for the virtual deformation energy corresponds to the plane of the material where fracture is

expected to occur. In case of multiaxial loading, this model considers two possible failure modes, traction failure mode W_I, and shear failure mode W_{II}.

$$DP_I = \Delta W_I = max(\Delta\sigma_n\Delta\varepsilon_n) + \Delta\tau\Delta\gamma \qquad (9)$$

$$DP_{II} = \Delta W_{II} = \Delta\sigma_n\Delta\varepsilon_n + max(\Delta\tau\Delta\gamma) \qquad (10)$$

5.4. MCC

MCC theory proposes that, for a given plane, the stress state can be decomposed into a normal and a shear component. During a complete loading cycle, the normal component remains perpendicular to the critical plane, varying only in intensity, while the shearing component describes a closed curve which, when projected in the critical plane, draws a circle with a radius Ra. Based on the criterion of Crossland and Sines, this method is formulated by the hydrostatic pressure P_H and the alternating shear stress amplitude. For the present study, the MCC criterion proposes that $\tau_a = R_a$.

$$DP = \tau_a + f.P_{Hmax} \qquad (11)$$

5.5. MCE

Taking into account the effects of non-proportionality, Freitas [14] introduces MCE model, which also circumscribes the trajectory of a load cycle. In phase loads, the stress vector can be represented in the critical plane by a straight line of constant length, which rotates around the origin along the cycle, eventually forming a circle (load path 1, figure 5.1). However, for out-phased loads, the line described by the stress vector has variable length over a cycle, describing an ellipse (load path 2, figure 5.1).
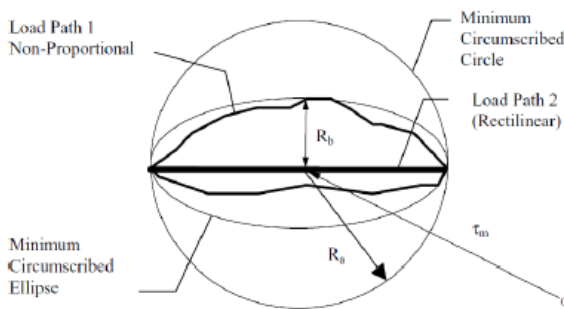

Figure 5.1–MCC and MCE comparison [14]

Thus, by the MCE model:

$$\tau_a = \sqrt{R_a^2 + R_b^2} \qquad (12)$$

Where Ra represents the largest radius of the ellipse and Rb the smallest.

6. Experiments and results

Tests are carried out at room temperature with load control, ensuring that the applied loads are equal in both direction and amplitude throughout all test $F_1 = F_2$. The frequency is kept at 20Hz and the tensions ratio $R = -1$. As consequence of using loadings with phase shifts, the loading paths lose the linear behavior and acquire a more complex one, figure 6.1.
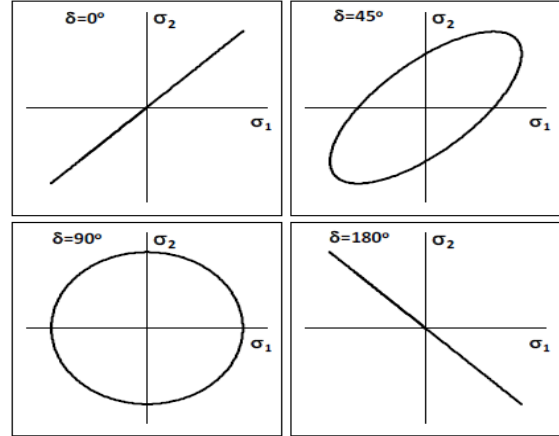

Figure 6.1 – Load paths

The crack growth by cyclic loads creates, in this specimen´s geometry, radial marks extending from the initiation zone to the final fracture zone. The figure belongs to specimen 013 and exemplifies the fracture surface of the BTM2023 specimens.
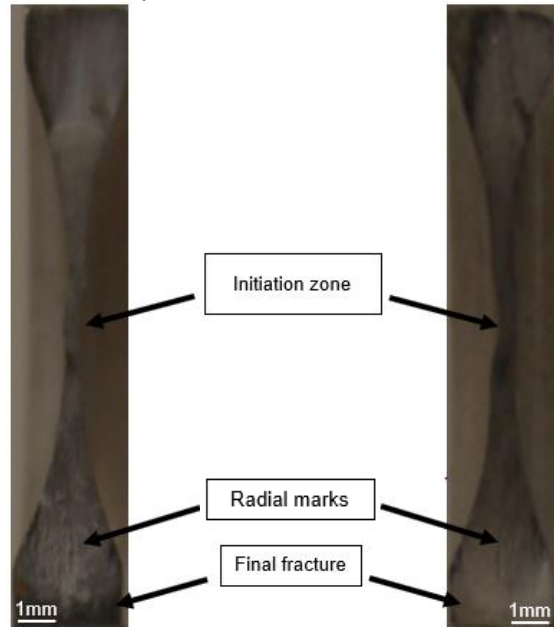

Figure 6.2 – Fracture surface, specimen 013

Table 6.1 – Test parameters and results

BTM	Tt (mm)	δ (º)	F(KN)	σ$_1$ (MPa)	σ$_2$ (MPa)	ε$_1$ (µε)	ε$_2$ (µε)	ε$_3$ (µε)	N$_f$	θ (º)
6	0,434	0	2,00	144,82	143,63	2300	2078	-1532	66703	Und.
12	0,443	0	2,10	150,70	149,48	2381	2169	-1593	46616	-13
13	0,446	0	2,00	142,99	141,84	2260	2058	-1511	63121	12
14	0,447	0	2,30	164,07	162,76	2594	2362	-1735	43178	14
16	0,445	0	2,05	149,26	148,07	2358	2148	-1577	52250	9
17	0,442	0	2,15	153,78	152,55	2432	2215	-1626	50671	3
18	0,441	45	1,70	142,80	139,61	3323	3170	-1195	87848	0
19	0,416	45	1,70	147,40	144,02	3426	3270	-1234	62249	2
20	0,442	45	1,68	142,56	139,36	3317	3164	-1194	61576	4
21	0,446	45	1,60	133,86	130,87	3115	2971	-1120	268491	-5
22	0,437	90	1,05	112,44	108,15	3289	3181	-563	113166	0
23	0,434	90	1,00	109,66	105,48	3207	3103	-549	1097885	0
24	0,44	90	1,08	118,17	113,66	3456	3343	-591	133396	3
25	0,447	180	0,90	121,72	116,01	3906	3793	-40	381959	0
26	0,446	180	0,95	129,61	123,53	4159	4038	-42	76308	-6
27	0,44	180	0,87	115,86	110,42	3718	3611	-38	105780	-1
29	0,445	0	2,2	151,01	149,71	2387	2176	-1597	81943	25
30	0,448	0	2,1	142,14	140,91	2245	2048	-1502	229195	27
31	0,447	45	1,7	129,40	130,95	3029	2792	-1135	98846	14
32	0,438	45	1,65	125,28	126,79	2932	2702	-1098	833530	Und.
33	0,444	90	1,2	110,88	115,16	3399	3144	-618	112124	8
34	0,445	90	1,1	102,80	106,77	3151	2915	-573	777453	5
35	0,441	180	1	110,09	116,23	3810	3528	-99	80426	0
36	0,433	180	0,9	98,72	104,22	3416	3164	-88	109597	0

Specimens 029 to 036 have a grain orientation inclined 15° from DL.

Table 6.1 shows the parameters and results of each test carried out for the various BTM specimens, describing the thickness of the specimen center Tt and the phase shift between loads δ. The values of stress, σ, and extension, ε, were collected through the FE models. These results, except for σ$_3$ that assumes null value in all tests, are presented in the following table by their maximum values. The crack propagation directions θ for each specimen, obtained from the direct analysis of the photos, are also presented in this table.

6.1. Crack initiation angle

From the results obtained in table 6.2, it can be seen that critical plane fatigue's criteria that account the shear parameters, τ and γ, namely the Findley, modified SWT and Liu II criteria, the angles of critical plane tend to ± 45º. This is because shear stresses are maximum for this value, however the normal parameters to the plane are minimal. This proves that, the shear parameters for these criteria have greater impact than the normal ones, since their variation is greater.

In the phase loading case, if material was considered isotropic, the normal tension would be constant and the shear stress would be null. However, conditions of anisotropy in magnesium can be verified, which implies that there is a small variation in normal and shear stress even for in-phase loading. However, this variation is too small and can be neglected, therefore the critical plane is undefined.

In table 6.2, the theoretical results are compared with the experimental crack initiation results. It is easy to verify that the SWT and Liu I theories are the criteria with the closest values to the results obtained experimentally. These models define the critical plane only based on the normal parameters and as such, the maximum values appear for planes orthogonal to the main loads. Given the above conditions, there is high probability that, for these planes, a mode I fracture will arise.

Table 6.2 – Results summary for crack initiation

Specimen with grain aligned to DL

Phase shift	Findley	SWT	SWT Mod	Liu I	Liu II	Experimental
0º	Und.	Und.	Und.	Und.	Und.	11º
45º	±45º	±90º/0º	±45º	±90º/0º	±45º	3º
90º	±45º	±90º/0º	±45º	±90º/0º	±45º	1º
180º	±50º	±90º/0º	±50º	±90º/0º	±45º	2º

Specimen with grain inclined 15º to DL

Phase shift	Findley	SWT	SWT Mod	Liu I	Liu II	Experimental
0º	Und.	Und.	Und.	Und.	Und.	26º
45º	±45º	±90º/0º	±45º	±90º/0º	±45º	14º
90º	±45º	±90º/0º	±45º	±90º/0º	±45º	7º
180º	±40º	±90º/0º	±40º	±90º/0º	±45º	0º

Table 6.3 – Criteria error

Phase shift	Findley (%)	SWT MOD (%)	LIU I (%)	Liu II (%)	MCC (%)	MCE (%)
0º	18,74	18,76	18,83	18,80	18,77	18,77
45º	41,66	35,86	33,75	55,76	44,01	32,96
90º	56,32	53,41	40,32	55,71	56,01	47,13
180º	90,47	46,56	41,35	51,64	46,66	47,62
Média	51,80	38,65	33,56	45,48	41,36	36,62

6.2. Life prediction

In order to understand criteria's ability to describe the specimen life, it was calculated the error of predictions against the tests results, by equation (13). Where $Life_{max}$ represents the highest value between life expectancy and experimental life of the specimen, $Life_{min}$ is the lowest value of the two. Afterwards, the average error was calculated per phase shift loads, table 6.3. Since during the study there was no significant variation between life predictions of specimens with grain aligned to DL and of specimens with grain inclined from 15º to DL, these were grouped by phase shifts.

$$Error\ (\%) = \frac{Life_{max} - Life_{min}}{Life_{max}} \times 100 \qquad (13)$$

According to figures 6.3 to 6.10, most criteria present some difficulty in predicting material life for specimens which have experienced close to 10^6 cycles. This limitation suggests that, for low applied biaxial stresses, the material exhibits more resistance to fracture than predicted by fatigue criteria. In Zeng study [15], it is found that for magnesium alloys subjected to low stress fatigue, the appearance of cracks is considerably conditioned by plasticity and formation of oxide films. Therefore, any micro-structural feature or oxide residue with a size comparable to crack opening

displacement will promote contact between the crack surfaces, which in turn closes the crack.

From the various critical plane methods, the best results were obtained for the modified SWT and Liu I criteria respectively. The modified SWT criterion had already been applied in the AZ61 magnesium alloy under conditions of multiaxial tensile-compression loads and pure torsion, obtaining excellent results [5]. Unlike the Liu I model, which accounts crack growth in failure mode I, the modified SWT criterion with b ~ 0.35 considers failure modes I and II.

For modified SWT, the value of λ, obtained from potential interpolation of points related to in-phase loads, figure 6.3, is 47,281. Thus, for this case we obtain:
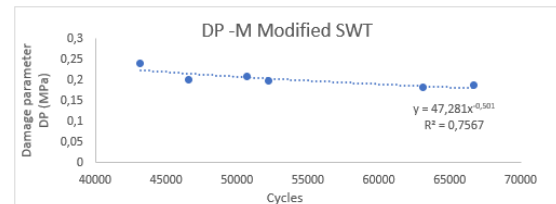
$$DP = 47,281 \times (2N_f)^{-0,501}$$

Figure 6.3 – DP-N modified SWT

In life prediction of this criterion, figure 6.4, most the points of the graphic are grouped in center for predictions minor to 10^6 cycles. Despite the divergence of these points, this criterion can present better results than the original SWT.
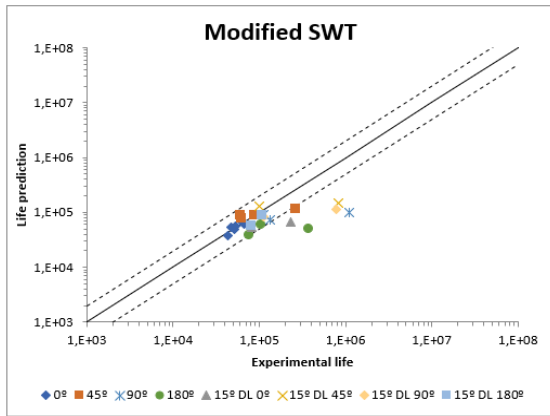
7

Figure 6.4 – Life prediction modified SWT

For Liu I criteria, the value obtained for λ parameter is given by 165,27, while b assumes the value of -0,5, therefore:

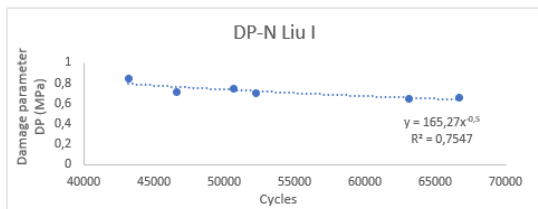$$DP = 165,27 \times (2N_f)^{-0,5}$$

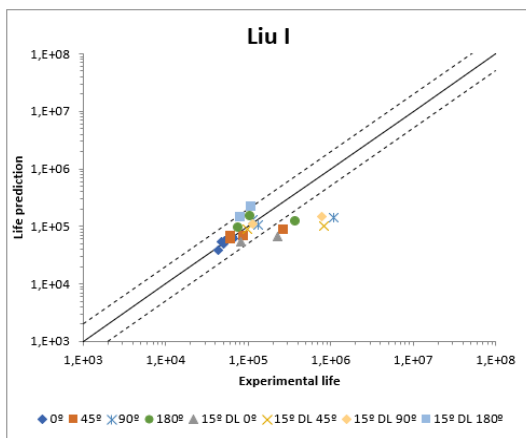

Figure 6.5 – DP-N Liu I

Figure 6.6 – Life prediction Liu I

Liu I criterion presents, in general, good results except for the points with experimental life close to 10^6 cycles

Of all the criteria, MCE and Liu I make the best predictions by grouping the various points in the central area of life prediction graphics, figure 6.6 and 6.8, respectively. The good correlation of the MCE criterion to conditions of multiaxial fatigue in the plane had already been verified for an aluminum alloy [7]. However, unlike this reference, the MCE criterion presents better results than MCC which would be expected from the beginning, given the higher accuracy of MCE for out-phase loads.

For this criterion, the expression is given by:

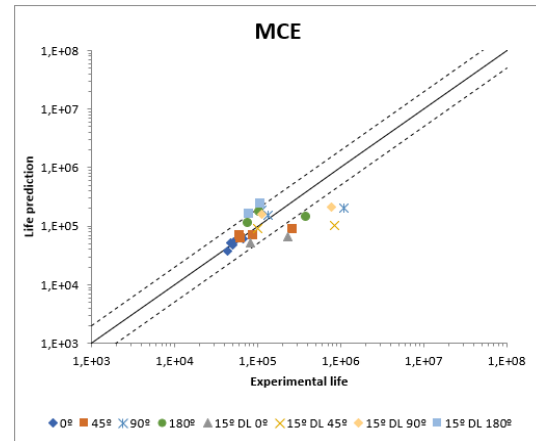$$DP = 2401(2N)^{-0,254}$$
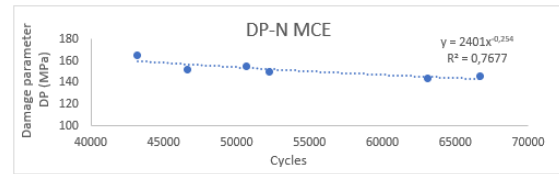
Figure 6.7 – DP-N MCE

Figure 6.8 – Life prediction MCE

This criterion presents relatively good results for the various phase shifts loads, despite points with experimental life close to 10^6 tend to be more conservative. On the opposite end, the Findley criterion gave the worst results, proving to be not adequate to make life predictions for the case in hands. This is visible from the high dispersion of points in figure 6.10.
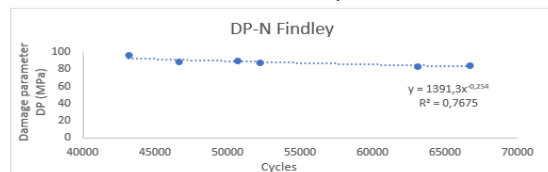
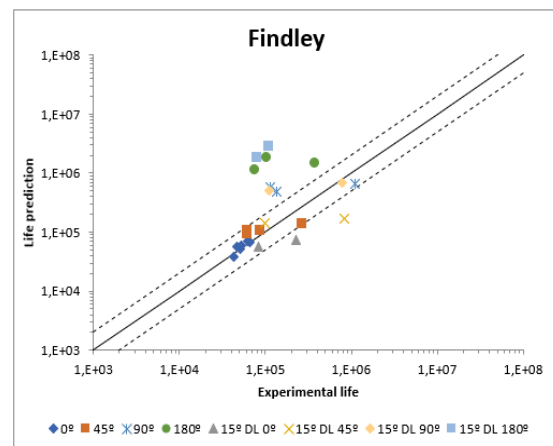$$DP = 1391,3(2N_f)^{-0,254}$$ 14

Figure 6.9 – DP-N Findley

Figure 6.10 – Life prediction Findley

6.3. Crack propagation

This chapter deals with crack evolution along the cycles and the respective tensile strength factor (SIF). While the crack length was obtained by direct analysis of the photographs, figure 6.11 and 6.12 exemplifies specimen 012, the SIF was removed by numerical study of each crack.
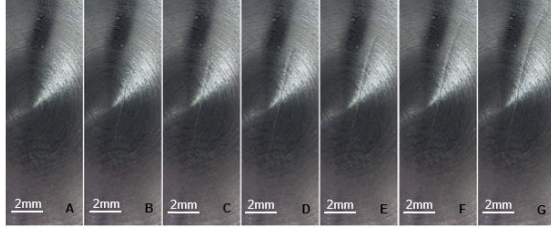
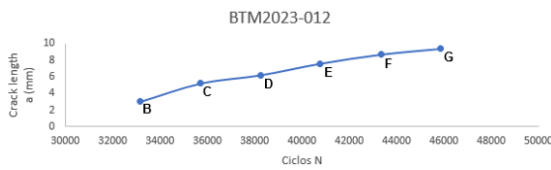

Figure 6.11 – Crack growth for specimen 012

Figure 6.12 – Crack growth graphic, specimen 012

The goal is to establish the Paris' equation and determine the respective constants, equation (14), by correlating the crack propagation rate with the equivalent SIF range. The presentation of results is presented according to phase shift loads.

$$\frac{da}{dN} = C \cdot \Delta K^m \qquad (14)$$

Where da/dN is the crack propagation rate, ΔK the stress intensity factor range, C and m are material constants.

As exemplified by specimen 12, most of the specimens propagated the crack along the initiation direction with a growth rate $\frac{da}{dN}$ which decreases slightly as the crack length increases. In a study [15] conducted on an alloy similar to the present, AZ91D, it has been found that crack interacts with grain boundaries and precipitates, where growth is retarded while increasing the plasticity of the crack front. After a few cycles the crack growth is resumed. Also, the geometry at the center of the specimen presents a progressive increase in thickness which will decrease the SIF value and, consequently, decrease the crack growth rate as the crack length increases. Thus, it is verified that the specimen does not present an optimal geometry for the study of crack propagation. However, to control this influence, the length of the crack was limited to the maximum length of a = 6mm. The figure 6.13, records the crack propagation of the various specimens.
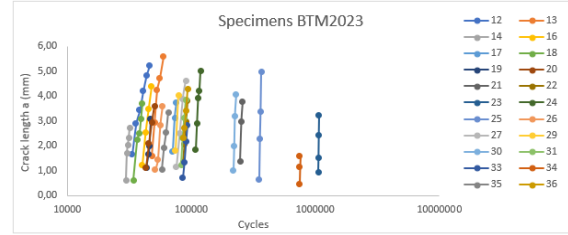

Figure 6.13 – Crack growth, BTM2023 specimens

For phase loading conditions, the points that correlate $\frac{da}{dN}$ with ΔK are plotted in figure 6.14, where an exponential trend line is added which relates the points in the same way as the Paris' law equation.
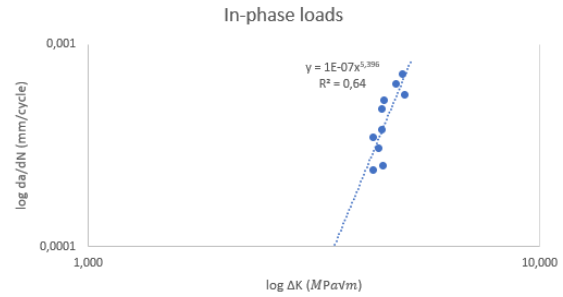

Figure 6.14 – da/dN vs ΔK_{eq}, in-phase loads

Several of the points obtained experimentally had to be disregarded in order to obtain in all correlations a coefficient of determination R^2 near 60%. The data for 45°, 90° and 180° out-phased loading conditions are shown in the crack propagation rate vs equivalent SIF range charts, from figure 6.15 to 6.17, respectively.

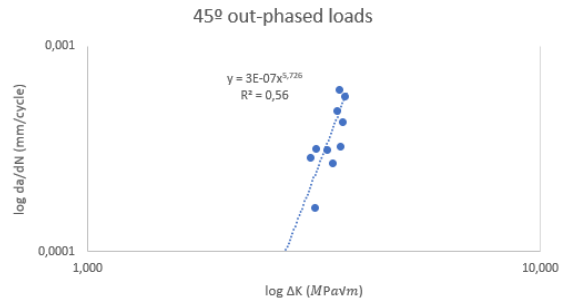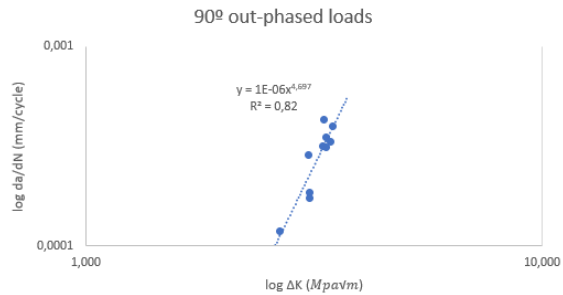*Figure 6.15 – da/dN vs ΔK_{eq}, 45° out-phased loads*

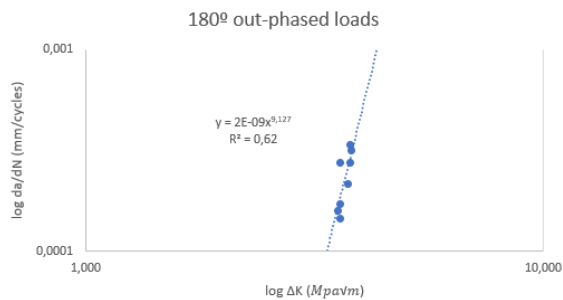*Figure 6.16 – da/dN vs ΔK_{eq}, 90° out-phased loads*

180º out-phased loads

$y = 2E-09x^{9,127}$
$R^2 = 0,62$

Figure 6.17 – da/dN vs ΔK_{eq}, 180º out-phased loads

The constants of the Paris' Law, namely C and m, obtained for the various loading conditions are summarized in table 6.4.

Table 6.4 – Results summary for crack propagation

Phase shift (º)	C (m/cycles)	m
0	$1,16 \times 10^{-10}$	5,396
45	$3,15 \times 10^{-10}$	5,726
90	$1,13 \times 10^{-9}$	4,697
180	$1,56 \times 10^{-12}$	9,127

Similar values to parameters C and m were obtained by the study [16] of an AZ61 magnesium alloy, which presents mechanical characteristics that resemble the alloy under study AZ31. In this study, for crack growth rate in the range of 10^{-7} to 10^{-9} m/cycles, under room conditions, it was determined the Paris' Law exponent m = 5. The study conducted by Venkateswaran [15] followed the behavior of crack growth in the AZ91D alloy, in which were determined lower values for m, in the value of 3.6. In other investigation [17] that analyzed crack growth in an AZ80 alloy, at a frequency of 10 Hz, it was obtained m = 2 and $C = 1.1 \times 10^{-9}$ m/cycles, arguing, however, that crack growth rate would increase to higher frequencies, which is supported by the results presented in this study. No documents were found to corroborate the values assumed by the Paris' Law in 180° out-phased loads, since they diverge significantly from the remaining values.

7. Conclusion

From the critical plan models being studied, only original SWT and Liu I criteria provided good estimates for crack initiation angle.

Life prediction criteria of Findley and Liu II have shown great difficulty in predicting fatigue life of biaxial loads. Liu I and MCE criteria revealed the best results of the study.

With exception of the constants obtained for 180º out-phased loads, the correlation between numerical and experimental data allowed to obtain acceptable Paris' law constants according to results obtained in similar alloys.

References

[1] C. Bettles e M. Barnett, "Advances in wrought magnesium alloys: fundamentals of processing, properties and applications.," *Woodhead Publishing,* 2012.

[2] D. Socie e G. Marquis, "Multiaxial fatigue," *SAE International,* 2000.

[3] Q. Yu, J. Zhang, Y. Jiang e Q. Li, "Effect of strain ratio on cyclic deformation and fatigue of extruded AZ61A magnesium alloy," *Int J Fatigue,* vol. 44, pp. 225-233, 2012.

[4] G. Chen, L. Lu, Y. Cui, R. Xing, H. Gao e X. Chen, "Ratcheting and low-cycle fatigue characterizations of extruded AZ31B Mg alloy with and without corrosive environment," *Int J Fatigue,* vol. 80, pp. 364-371, 2015.

[5] Q. Yu, J. Zhang, Y. Jiang e Q. Li, "Multiaxial fatigue of extruded AZ61A magnesium alloy," *Int J Fatigue,* vol. 33, pp. 437-447, 2011.

[6] J. Albinmousa, H. Jahed e S. Lambert, "Cycli behaviour of wrought magnesium alloy under multiaxial load," *Int J Fatigue,* 2011.

[7] J. Fonseca, "Previsão de vida à fadiga em carregamentos biaxiais não proporcionais," *Instituto Politécnico Setubal,* 2013.

[8] R. Baptista, R. Cláudio, L. Reis, I. Guelho, M. Freitas e J. Madeira, "Design optimization of cruciform specimens for biaxial fatigue loading," *Frattura ed Integritá Strutturale,* vol. 30, pp. 118-126, 2014.

[9] I. Guelho, L. Reis, M. Freitas, B. Li, J. Madeira e R. Cláudio, "Optimization of Cruciform Specimen for a Low capacity Biaxial Testing Machine," *10th International Conference on Mechanical Fatigue & Fracture,* 2013.

[10] R. Cláudio, L. Reis e M. Freitas, "Biaxial high-cycle fatigue life assessment of ductile aluminium cruciform specimens," *Theoretical and Applied Fracture Mechanics,* vol. 73, pp. 82-90, 2014.

[11] M. Freitas, L. Reis, B. Li, I. Guelho, V. Antunes, J. Maia e R. Cláudio, "In-Plane Biaxial Fatigue Testing Machine Powered by Linear Iron-Core Motors," *Application of Automation Technology in Fatigue and Fracture Testing and Analysis,* vol. 6, pp. 63-79, 2014.

[12] H. Richard, M. Fulland e M. Sander, "Theoretical crack path prediction," *Fatigue & Fracture of Engineering Materials & Structures,* vol. 28, pp. 3-12, 2005.

[13] Y. Jiang e H. Sehitoglu, "Fatigue and stress analysis of rolling contact," *College of Engineering, University of Illinois at Urbana-Champaign,* 1992.

[14] M. Freitas, B. Li e J. Santos, "A numerical approach for high-cycle fatigue life prediction with multiaxial loading," *Multiaxial Fatigue and Deformation: Testing and Prediction,* pp. 139-156, 2000.

[15] R. Zeng, Y. Xu, W. Ke e E. Han, "Fatigue crack propagation behavior of an as-extruded magnesium alloy AZ80," *Materials Science and Engineering,* vol. 509, pp. 1-7, 2009.

[16] P. Venkateswaran, S. Ganesh, S. Pathak, Y. Miyashita e Y. Mutoh, "Fatigue crack growth behaviour of a die-cast magnesium alloy AZ91D," *Materials Letters,* vol. 58, pp. 2525-29, 2004.

[17] U. Karr, A. Stich e H. Mayer, "Very high cycle fatigue of wrought magnesium alloy AZ61," *Procedia Structural Integrity,* vol. 2, pp. 1047-1054, 2016.